Electrochimica Acta 145 (2014) 177–184

Contents lists available at ScienceDirect

Electrochimica Acta

journal homepage: www.elsevier.com/locate/electacta

Unveiling the dynamic capacitive storage mechanism of Co_3O_4 @$NiCo_2O_4$ hybrid nanoelectrodes for supercapacitor applications

Yonghe Li[a], Yuefei Zhang[a,*], Yujie Li[a], Zhenyu Wang[a], Haoyu Fu[a], Xiaona Zhang[a], Yanhui Chen[b], Hongzhou Zhang[b], Xiaodong Li[a,c,*]

[a] Institute of Microstructure and Property of Advanced Materials, Beijing University of Technology, Beijing 100124, P. R. China
[b] School of Physics and Centre for Research on Adaptive Nanostructures and Nanodevices (CRANN), Trinity College Dublin, Dublin 2, Republic of Ireland
[c] Department of Mechanical and Aerospace Engineering, University of Virginia, Charlottesville, Virginia 22904, United States

ARTICLE INFO

Article history:
Received 24 April 2014
Received in revised form 10 June 2014
Accepted 30 June 2014
Available online 30 July 2014

Keywords:
$NiCo_2O_4$
Co_3O_4
Capacitance activation
Supercapacitor

ABSTRACT

We report a simple and cost-effective approach to the synthesis of hierarchical mesporous Co_3O_4@$NiCo_2O_4$ nanoforests on Ni foam for supercapacitor (SC) electrode applications by a coupled one-step solution and annealing process. The synthesized electrode exhibits capacitive activation during charge-discharge cycling (from 0.73 F/cm^2 of the pristine state to the peak value of 1.12 F/cm^2 after 2000 cycles with only 1.8% loss compared to the peak capacitance after another 2000 cycles). We attribute such dynamic capacitive activation to (1) enlarged electroactive surface area through the formation of Co_3O_4@$NiCo_2O_4$ core-shell structure and (2) enhanced electrical conductivity by forming oxygen vacancies and hydroxyl groups during charge-discharge cycling. Our findings provide a scientific explanation for the capacitive activation in cobalt oxide-binary nickel cobaltite compounds, and a new design guideline for the development of capacitive activation enabled, high performance transitional oxide electrodes.

1. Introduction

To meet urgent needs for sustainable and renewable power sources for high power electronic devices, back-up power supplies and electric vehicles, many efforts have been made in developing high performance batteries [1,2] and supercapacitors [3–5]. Traditional lithium-ion batteries suffer from a somewhat slow power delivery or uptake [6]. Faster and higher power energy storage systems are critical in a number of applications, such as uninterruptible power suppliers (back-up supplies used to protect against power disruption) and airplane emergency doors, and this task has been assigned to supercapacitors [3]. Supercapacitors, also called ultracapacitors or electrochemical capacitors (ECs), have become some of the most promising candidates for next-generation power devices because of their overall advantages of high power density, fast charging/discharging rate, sustainable cycling life (millions of cycles) and excellent cycle stability [3,4]. Many materials have been explored for supercapacitor electrodes, including carbon-based materials, conducting polymers, and both noble and transition metal oxides. Among these candidate electrode materials, transition metal oxides, such as NiO, [7,8] V_2O_5, [9] MnO_2, [10–12] etc, have attracted tremendous interest due to their low cost, high energy density, and environmental friendliness. Of particular interest, spinel cobalt oxides and binary nickel cobaltite compounds exhibit many exceptional characteristics, such as good redox activity, high capability and extremely high theoretical specific capacitance (3560 F/g), [13,14] suggesting them as the most promising electrode materials for next generation supercapacitors.

With all the excitment about new electrode materials, less attention has been paid to their dynamic stoage mechanims. It has been shown that nanomaterials of Co_3O_4 [15–20] and $NiCo_2O_4$ [21–29] exhibit intriguing capacitive activation during charge/discharge cycling. In the first cycle, only a fraction of the material is active, whereas in the subsequent cycles the electrolyte gradually penetrates into the nanomaterials, pushing up the capacitance to a higher level [15–29]. However, the mechanisms for such enhanced cycling capacitance remain, to a large extent, unknown. Several key questions are rasied, yet left unanswered: What structural morphology renders the electrode such enhanced cycling capacitance? Does the microstrucure of the electrode change during charge-discharge cycling? Does charge-discharge cycling generate new structure and/or materials? In this context, we have

* Corresponding author.
E-mail addresses: yfzhang@bjut.edu.cn (Y. Zhang), xl3p@virginia.edu (X. Li).

http://dx.doi.org/10.1016/j.electacta.2014.06.168
0013-4686/

a pressing need for a fundamental understanding of the correaltion between the capacitive activation and microstructure of Co_3O_4 and $NiCo_2O_4$ electrodes during charge-discharge cycling.

In this paper, we report a simple and cost-effective approach to the synthesis of hierarchical mesporous Co_3O_4@$NiCo_2O_4$ nanoforests on Ni foam for SC electrode applications by a coupled one-step solution and annealing process. The synthesized electrode exhibits capacitive activation during charge-discharge cycling (from 0.73 F/cm^2 of the pristine state to the peak value of 1.12 F/cm^2 after 2000 cycles with only *ca.*1.8% loss compared to the peak capacitance after another 2000 cycles). We attribute such dynamic capacitive activation to (1) enlarged electroactive surface area through the formation of Co_3O_4@$NiCo_2O_4$ core-shell structure and (2) enhanced electrical conductivity by forming oxygen vacancies and hydroxyl groups during charge-discharge cycling. Our findings provide a scientific explanation for the capacitive activation in cobalt oxide-binary nickel cobaltite compounds, anda new design guideline for the development of capacitive activation enabled, high performance transitional oxide electrodes.

2. Experimental section

2.1. Materials synthesis

All solvents and chemicals were of reagent quality and were used without further purification. Cobalt nitrate, ammoniumfluorideand urea were obtained from Beijing Chemical Reagent Co. In a typical synthesis, $Co(NO_3)_2{\cdot}6H_2O$ (2 mmol), NH_4F (8 mmol) and $CO(NH_2)_2$ (2 mmol) were dissolved in distilled water (40 mL) to form pink homogeneous solution. Then the homogeneous solution prepared above was transferred into Teflon-lined stainless steel autoclave liners (50 ml). Then, a piece of clean nickel foam (2 cm × 1 cm) was immersed into the reaction solution. The top of the foam (1 cm × 1 cm in area) was protected from solution contamination by uniformly coating the top with a polytetrafluoroethylene tape. The liner was sealed in a stainless steel autoclave and then held at 120 °C for 6 h. To study the growth mechanism, intermediate products were also obtained at the reaction time periods of 30 min, 45 min, 1 h, 3 h and 6 h. The Ni foam coated with a pink colour precursor was collected and rinsed with distilled water and ethanol several times before drying at 80 °C under vacuum for 2 h. Finally, the precursor was annealed at 300 °C in ambient atmosphere for 3 h, producing Co_3O_4@$NiCo_2O_4$ nanoforests.

2.2. Structural characterization

The crystal structure of the as-synthesized samples were characterized by X-ray diffraction (XRD, SHIMADZU XRD-7000) using a CuK_α source (λ = 0.154056 nm) with step size of 0.02°. Energy dispersive X-ray spectrometry (EDS) with FEI Tecnai G20 was carried out to determine the molar ratio of the products. The morphology and structure of the prepared precursors and final products were studied by field emission scanning electron microscopy (FESEM, FEI Quanta 600 with an accelerating at 20 kV), and transmission electron microscopy (TEM, FEI Tecnai G20 with an accelerating at 200 kV), high-resolution transmission electron microscopy (HRTEM, JEOL JEM-2010F with an accelerating at 200 kV), and Fourier transform infrared spectroscopy (FTIR, Nicolet 6700 spectrophotometer).The *in-situ* electrical measurement experiments were performed using a commercial scanning tunneling microscope-transmission electron microscope (STM-TEM, Nanofactory Instruments) joint instrument insert into JEOL-2010 TEM. The chemical composition and oxidation state were characterized by Electron energy loss spectroscopy (EELS, FEI Titan 80-300(S)operating at 300 kV) and X-ray photoelectron spectroscopy (XPS, PHI Quantera SXM with Al K_α radiation).

2.3. Electrochemical tests

The electrochemical measurements were carried out at room temperature in a three–electrode electrochemical cell containing 6 M KOH aqueous solution as electrolyte. Cyclic voltammetry (CV) measurements were performed with a PARSTAT2273 electrochemical workstation (Ametek, America), the Co_3O_4@$NiCo_2O_4$ nanoforest–Ni foam composite (1 cm^2 in area) as the working electrode, Hg/HgO as the reference electrode and Pt foil as the counter electrode. The galvanostatic charge-discharge tests were conducted using a LAND battery test system (Land, Wuhan). Electrochemical impedance spectroscopy (EIS) was carried out at open circuit potential with an ac perturbation of 5 mV in the frequency range of 100 kHz–0.01 Hz.

3. Results and discussion

Fig. 1 shows the structural characteristics of the as-prepared hybrid Co_3O_4@$NiCo_2O_4$ nanoforest–Ni foam composite. Fig. 1a presents the typical XRD spectrum of the as-prepared product. The diffraction peaks, except for the three typical peaks from the Ni foam, can be indexed to spinel Co_3O_4 (JCPDS no 42-1467) and $NiCo_2O_4$ (JCPDS no 20-0781), which originated from the respective Co(OH)F precursor and (Ni, Co) $(CO_3)_{0.5}(OH){\cdot}0.11H_2O$ precursor (see Fig. S1 in Supporting Information for details). The SEM images (Fig. 1b-c) reveal that the Co_3O_4@$NiCo_2O_4$ nanoforests were radially grown on the Ni foam. The nanoforests (Fig. 1d) exhibit a hierarchical nanorod@nanoneedle architecture with a clear boundary between the nanorod segment and nanoneedles (indicated by the dash line in Fig. 1d). The evolution process of the hierarchical nanoforests at different reaction stages can be found in Fig. S2 in Supporting Information. The EDS result (Fig. 1e and f) further unveil that the cycled area e' in Fig. 1d is rich in Co and O (Fig. 1e)with the ratio close to that of Co_3O_4. Note that Cu peaks came from the TEM grid and the small Ni peak originated from the Ni foam. Ni, Co and O were detected (Fig. 1f) in the corresponding cycled area f' (see Fig. 1d) and their atomic ratio is close to that of $NiCo_2O_4$. The EDS results validate the findings from the XRD in Fig. 1a. The close-up TEM view (Fig. 1g) reveals that an individual $NiCo_2O_4$ nanoneedle consists of nanoparticles that are assembled into the mesporous structure, which should facilitate electrolyte and electron transport. The crystalline $NiCo_2O_4$ nanoparticles have a size of 10 nm and the inter-particle mespores range from 2 to 5 nm in size. Fig. 1i shows the close-up HRTEM image of the single nanoparticle selected from Fig. 1h, revealing that both d-spacings of 0.203 nm are attributed to the (400) and (040) crystal planes of spinel cubic $NiCo_2O_4$, respectively. Fig. 1j presents the EDS elemental maps of Co_3O_4@$NiCo_2O_4$ nanoforest, showing that the elements of Ni, Co are uniformly distributed in the nanoforest. To better describe the elemental distributions, we used a dash line to indicate the boundary between the nanoneedles and the nanorod segment. Cleary, Co and O are rich in the nanorod segment. A small amount of Ni in the nanorod segment originates from the Ni foam. Ni, Co and O are homogeneously distributed in the nanoneedle part.

Cyclic votalmmetry (CV) tests were performed on the mesporous Co_3O_4@$NiCo_2O_4$ nanoforest–Ni foam composite. It is of interest to note that it takes approximately 2000 cycles for the mesporous Co_3O_4@$NiCo_2O_4$ nanoforest–Ni foam composite to achieve the peak capacitance. The CV curves of the 1st cycle and after 4000th cycle at a scan rate of 5 mV/s are depicted in Fig. 2a for comparison. The enclosed separation area was much increased after 4000 cycles. Both curves exhibit a pair of broad redox peaks, which are the

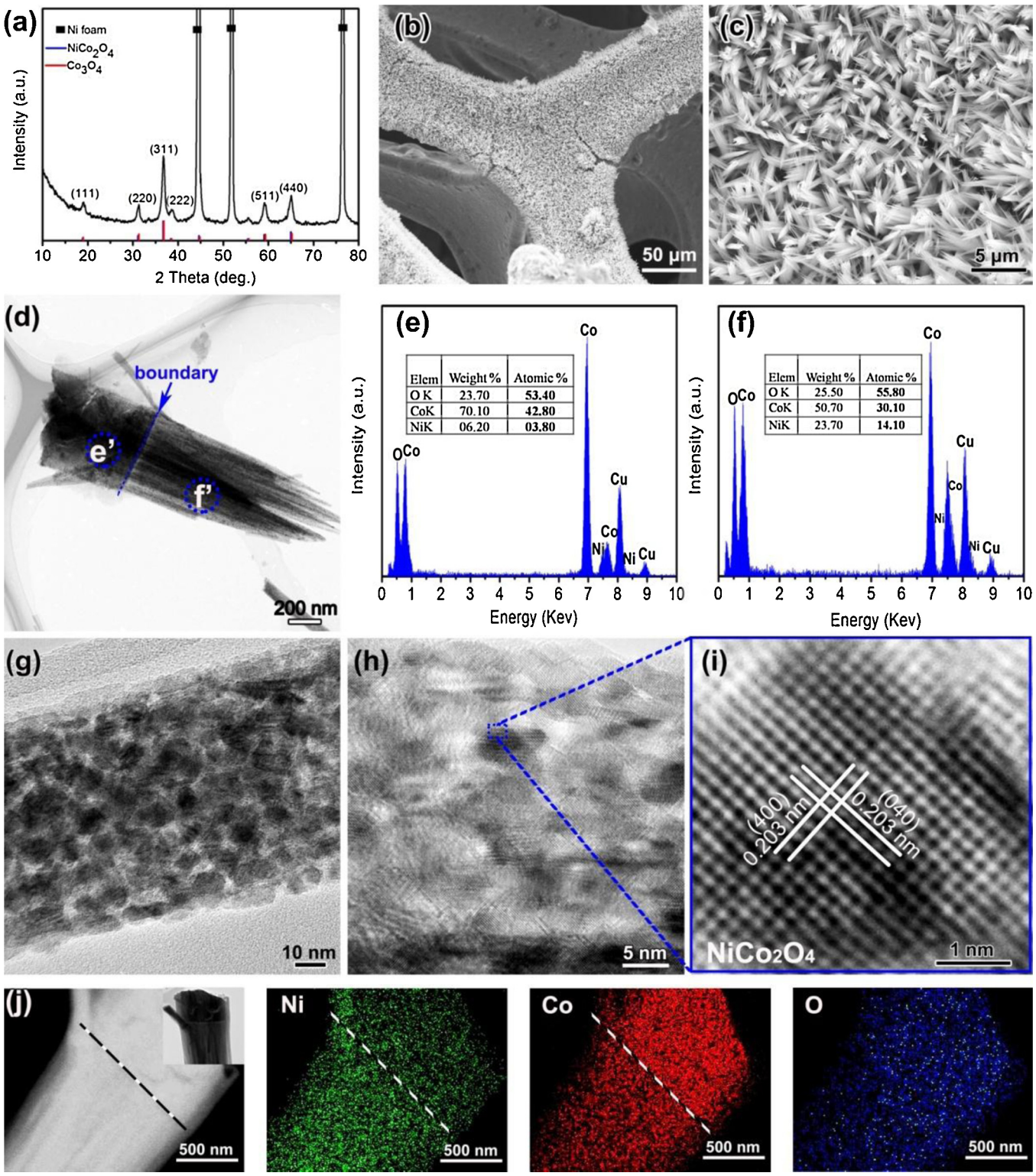

Fig. 1. Structural characterization of mesporous Co_3O_4@$NiCo_2O_4$ nanoforest–Ni foam composite. (a) XRD pattern of the as-prepared Co_3O_4@$NiCo_2O_4$ nanoforest–Ni foam composite. (b, c) SEM images of Co_3O_4@$NiCo_2O_4$ nanoforests grown radially on the Ni foam. (d) TEM image of a single Co_3O_4@$NiCo_2O_4$ nanoforest, showing the typical hierarchical nanorod@nanoneedle structure and (e, f) the corresponding EDS spectra taken from areas e' and f' in (d). (g) HRTEM image of individual $NiCo_2O_4$ nanoneedles, showing mesporous structure and (h, i) the corresponding lattice-resolved HRTEM images. (j) Energy dispersive X-ray spectroscopy (EDS) element mapping images of the Co_3O_4@$NiCo_2O_4$ nanoforest, showing Ni, Co, and O distribution.

characteristic peaks of faradic reaction for M-O/M-O-OH (M represents Ni or Co) in KOH electrolyte [15,22].

Rate capability is one of the important factors to evaluate the power applications of SCs. The galvanostatic charge-discharge curves and calculated specific capacitance of the as-prepared Co_3O_4@$NiCo_2O_4$ nanoforest–Ni foam composite at different discharge current densities are shown in Fig. 2b-c. The pristine Co_3O_4@$NiCo_2O_4$ nanoforest–Ni foam composite exhibits a

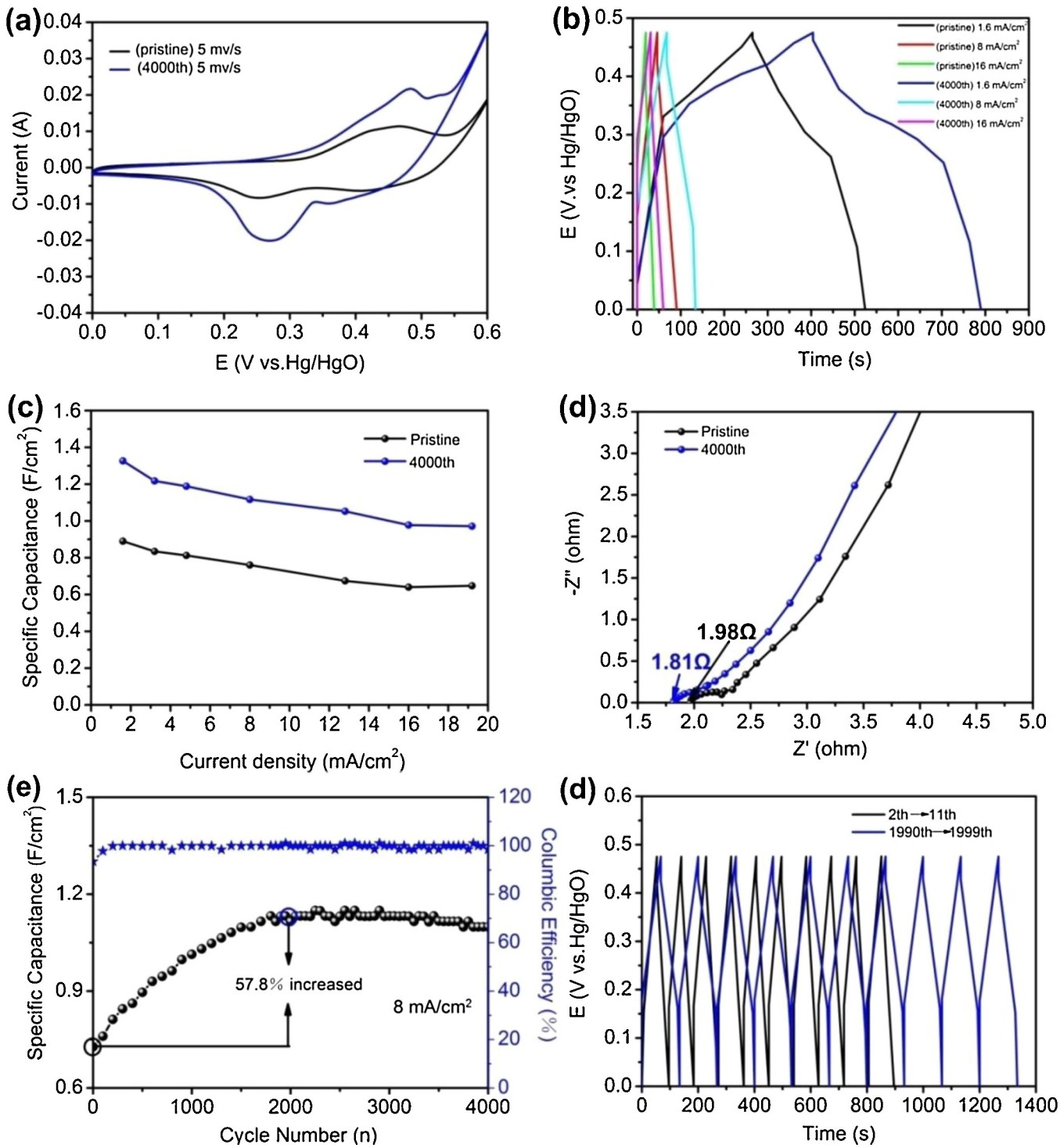

Fig. 2. Electrochemical performance of mesporous Co_3O_4@$NiCo_2O_4$ nanoforest–Ni foam composite. (a) CV curves, (b) Galvanostatic charge-discharge curves, (c) Comparison in specific capacitance of pristine sample and the sample after 4000 galvanostatic charge-discharge cycles, showing dramatically improved capacitance after sufficient activation. (d) Nyquist plots of pristine sample and the sample after 4000charge-discharge cycles. (e) Cycling performance and columbic efficiency at current density of 8 mA/cm^2, showing 57.8% increased capacitance after 2000 cycles compared to the pristine pattern. (f) Galvanostatic charge-discharge curves of 2th-11th and 1990th-1999th cycles.

pseudocapacitance of 0.89 F/cm^2 at 1.6 mA/cm^2. After 4000 cycles, the specific capacitance was pushed up to 1.32 F/cm^2 at 1.6 mA/cm^2 (measured at the cyclic current density of 8 mA/cm^2). The Co_3O_4@$NiCo_2O_4$ nanoforest–Ni foam composite also shows good rate capability (*ca.*73% retention at 12 times higher current density with reference to 0.97 F/cm^2 at current density of 19.2 mA/cm^2). The obtained Nyquist plots are shown in Fig. 2d. Both EIS curves consist of a depressed arc in the high frequency region and an inclined line in the low frequency region. The value of R_s (internal resistance) of the pristine electrode is 1.96 Ω. Notably, after 4000th cycle, the R_s value decreased down to 1.81 Ω, showing that the electron conductivity of the electrode increased after long-term cycling. Such an enhancement in the electronic conductivity is probably another important factor for the fact that activation takes a certain

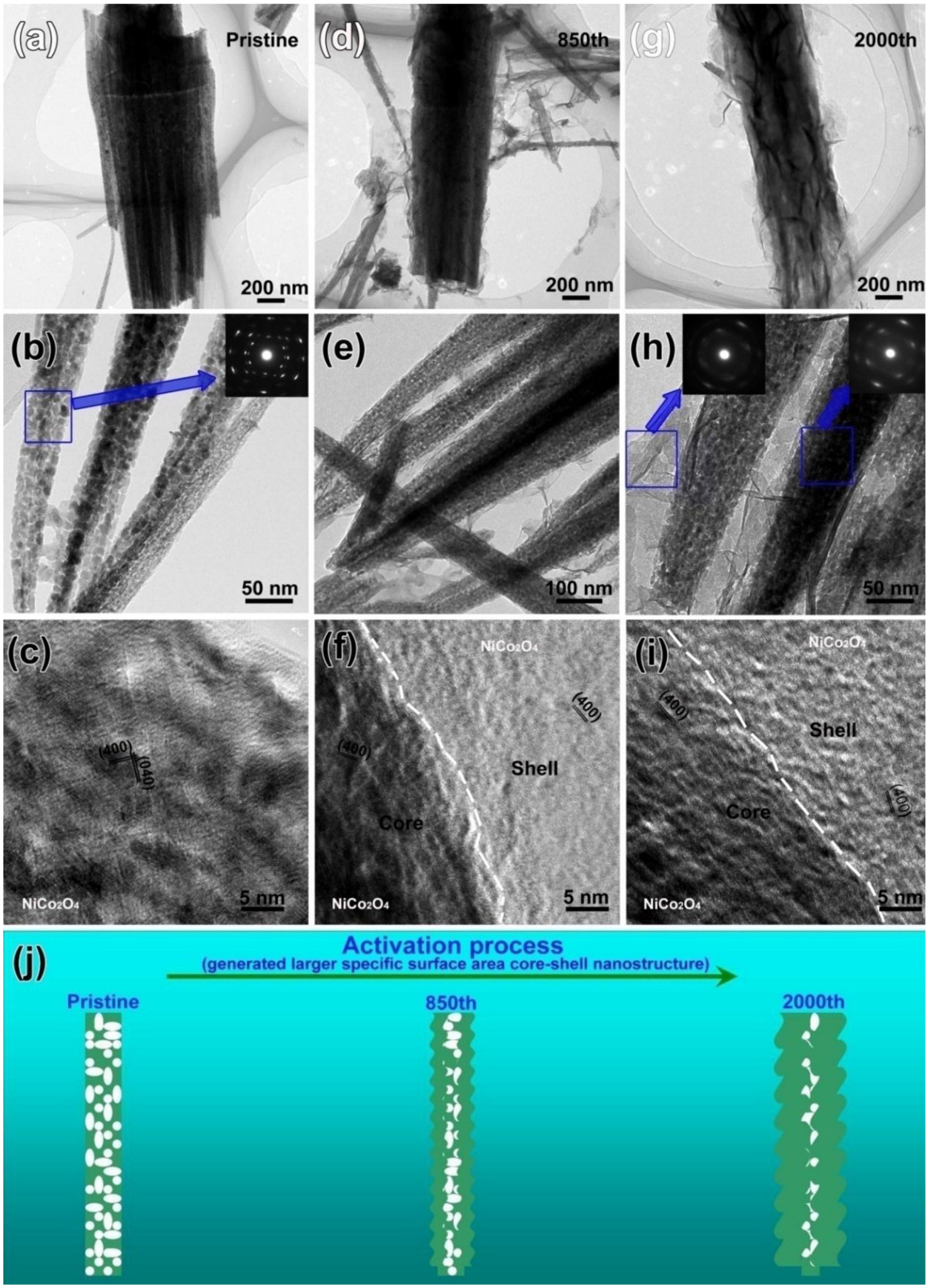

Fig. 3. Ex-situ HRTEM characterization of (a, b, c) pristine, (d, e, f) 850th cycle and (h, i, g) 2000th cycle at current density of 8 mA/cm^2, the insets are the corresponding SAED patterns. (j) Schematic illustration of morphology evolution of Co_3O_4@$NiCo_2O_4$ nanoforests during activation process.

period of time to occur. Accordingly, the R_{ct} (pseudo charge transfer resistance) changed subtly after 4000 cycles, demonstrating the good retention capability.

The charge-discharge cyclic stability of the Co_3O_4@$NiCo_2O_4$ nanoforest–Ni foam composite was also tested at 8 mA/cm^2. As can be seen in Fig. 2e, the cycling period can be largely divided into two regimes, i.e. the active stage and the stable stage. In the active stage, specific capacitance increased 57.8% from 0.73 F/cm^2 of the 1st cycle to the peak value of 1.12 F/cm^2 of the 2000th cycle. The stable stage, i.e. the period ofthe 2000th cycle to the 4000th cycle, characterizes a slow rate of decrease in specific capacitance from the peak value of 1.12 F/cm^2 down to 1.1 F/cm^2 of the 4000th cycle, 98.2% retention rate with reference to the peak value. The cycling performance of Co_3O_4@$NiCo_2O_4$ nanoforest arrays is much better than that of the other Co_3O_4 and $NiCo_2O_4$-based nanostructures, such as $NiCo_2O_4$@MnO_2 core/shell nanowire arrays (12% loss after 2000 cycles), [39] hierarchical porous $NiCo_2O_4$ nanowires (~6.2% loss after 3000 cycles), [22] Co_3O_4@$NiMnO_4$ nanowire arrays (~23% loss after 3000 cycles), [40] $NiCo_2O_4$ nanowires (~19% loss after 3000 cycles) [41]. The columbic efficiency of the electrode in all cycling periods maintained nearly at 100%, showing an excellent reversibility of the electrode. Fig. 2f shows the charge-discharge curves of 2th-11th cycles and 1990th-1999th cycles. It can be seen that both curves still kept near linear and symmetrical shape, and charge-discharge time prolonged after 1990th-1999th cycles, implying that capacitive activation occurred.

To seek the underlying mechanism of the observed enhancement in specific capacitance during charge-discharge cycling, the crystal structure and morphology evolution of the electrode at different activation stages were characterized by XRD and HRTEM. Comparison of the XRD spectra of the 1st cycle and the 2000th cycle at the current density of 8 mA/cm^2 (see Fig. S3a in Supporting Information) suggests that phase transformation would not occur during this cycling period. Fig. 3a presents the TEM image of the pristine Co_3O_4@$NiCo_2O_4$ nanoforests, showing a typical hierarchical mesporous nanorod@nanoneedle structure. The close-up view (Fig. 3b) reveals that individual nanoneedles consist of numerous nanoparticles which have $NiCo_2O_4$ crystal structure (see the insert of Fig. 3b and the XRD pattern of Fig. S3a in Supporting Information). The HRTEM image of the nanoparticles (Fig. 3c) reveals that the d-spacings of both 0.203 nm crystal planes correspond to the (400) and (040) planes of cubic $NiCo_2O_4$, respectively. TEM images (Fig. 3d-e) further reveal that after 850th charge-discharge cycle, the Co_3O_4@$NiCo_2O_4$ nanoforests were uniformly covered with a 20-50 nm length layer, forming a core-shell nanostructure (see Fig. 3f). This layer consists of $NiCo_2O_4$ nanocrystalsof 2-5 nm in size originating from the core part of nanoneedles (see Fig. S 3b in Supporting Information), which in turn suppresses the volume change of electrode during electrochemical de/alloying, leading to the inhibition of cracking and pulverization [30]. The measured-spacings of the (400) crystal planes in both core and shell are in consistent with the d-spacing of spinel cubic $NiCo_2O_4$. The TEM images of the sample after 2000th cycle (Fig. 3g-i) show that the shell layer grew to a length of *ca.* 100-200 nm, uniformly covering nanoforests to form Co_3O_4@$NiCo_2O_4$ core-shell structure with an enlarged surface area. The SAED patterns (insets in Fig. 3h) and the same d-spacings (Fig. 3i) show that both the core and shell have the same $NiCo_2O_4$ crystal structure. A schematic illustration (Fig. 3j) illustrates the morphology evolution and benefits of the Co_3O_4@$NiCo_2O_4$ nanoforests during the activation process. The nanoflake shells enable the full exposure of both active Co_3O_4 and $NiCo_2O_4$ to the electrolyte, thus enhancing both ion and electron diffusion [17,23]. The overall experimental evidences conclude that the self-developed core-shell structure with enhanced electrochemical sites facilitates the activation process.

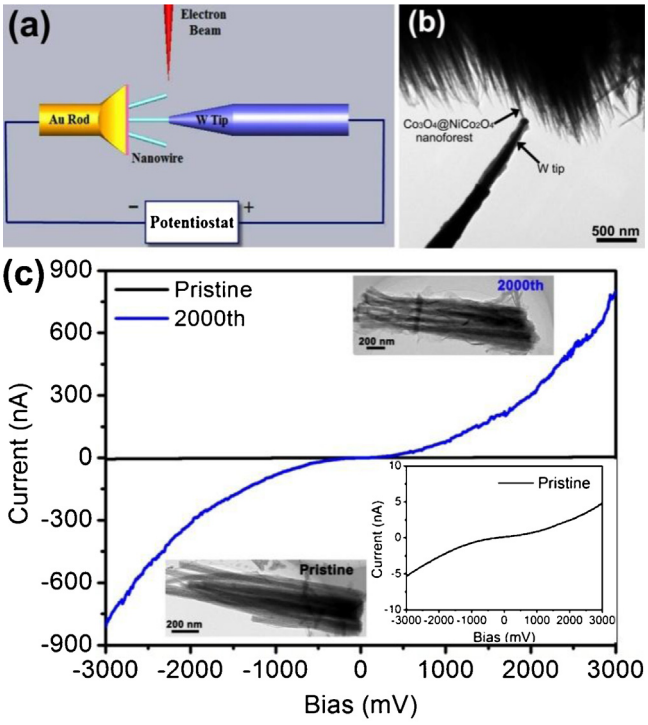

Fig. 4. (a) Schematic representation of *in-situ* STM-TEM conductivity test device. (b) TEM view of the framed area where an individual Co_3O_4@$NiCo_2O_4$ nanoforest mounted between a W tip and an Au rod. (c) *I-V* characteristics of single Co_3O_4@$NiCo_2O_4$ nanoforest of pristine sample and the sample after 2000 charge-discharge cycles at 8 mA/cm^2, insets are corresponding TEM images.

To understand the obtained *I-V* curves under different cycles (1st cycle and 2000th cycle), the electrical conductivity of the as-prepared Co_3O_4@$NiCo_2O_4$ nanoforests was studied *in-situ* using a Nanofactory Instruments scanning tunnelling microscope (STM)-transmission electron microscope (TEM) electrical probing system. An experimental setup is sketched in Fig. 4a. An Au rod was attached to a fixed electrical sensor, and the as-synthesized Co_3O_4@$NiCo_2O_4$ nanoforest sample was adhered to the piezo-movable side of Au rod. Then the position of the W tip and an individual Co_3O_4@$NiCo_2O_4$ nanoforest were coordinatively adjusted through the nanoscale precision piezo-driven manipulator of STM-TEM holder to realize a bridge (Fig. 4b). The electrical properties (*I–V* curves) of this bridged Co_3O_4@$NiCo_2O_4$ nanoforest were measured, as shown in Fig. 4c. The current value of the pristine Co_3O_4@$NiCo_2O_4$ nanoforest varies from -5.23 nA to 4.8 nA, while after charge-discharge 2000 cycles at 8 mA/cm^2, the current value varies from -805.7 nA to 801.6 nA. The cycled Co_3O_4@$NiCo_2O_4$ nanoforest possesses more than two orders of magnitude electrical conductivity compared with the pristine one, which could significantly improve the pseudocapacitance based on Faradic reaction process during charge-discharge cycling.

The structural evoluation of the Co_3O_4@$NiCo_2O_4$ nanoforest during charge-discharge cycling was studied by *in-situ* electron energy loss spectroscopy (EELS) (Fig. 5). Fig. 5a-b show the L_3/L_2 lines ratios for Co L-edge and Ni L-edge (determined by directly integrating the individual peaks [31]). The calculated L_3/L_2 ratios for Co L-edge and Ni L-edge in the pristine pattern are 1.8 and 2.0, respectively, while the correpsonding ratios respectively increased to 2.8 and 2.2 for the samples after 2000 cycles. The increased average (Co, Ni) L_3/L_2 ratio indicates a valence decrease of Co (Co^{3+} to Co^{2+}) while a little change of Ni^{3+} to Ni^{2+} [32] after 2000 charge-discharge cycles. This findings validated by the change of oxygen K-edge structure. The O K-edges for the pristine sample and the

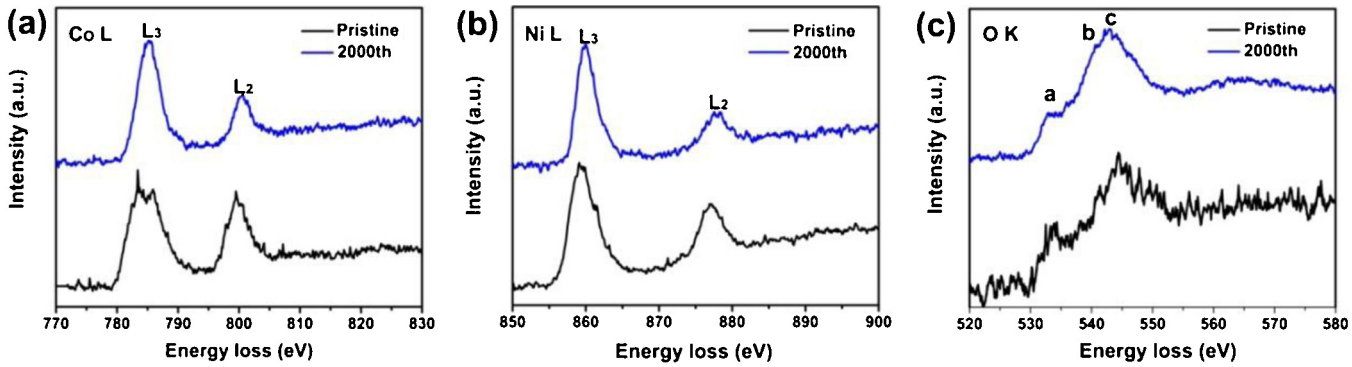

Fig. 5. Valence states and defect characterization of Co_3O_4@$NiCo_2O_4$ nanoforests for pristine sample and the sample after 2000 charge-discharge cycles at 8 mA/cm^2. EELS spectrums of (a) Co $L_{2,3}$-edges, (b) Ni $L_{2,3}$-edges and (c) O K-edge.

sample after 2000 cycles (Fig. 5c) show three characteristic peaks, labeled correspondingly as *a*, *b* and *c*. Peak *a* located in 532.7 eV is referred to as the O K-edge pre-peak, which is attributed to the hybridization of O 2*p*-state with the transition metal-3*d*, and is correlated with the 3d-band unoccupied of transition metal [35]. Peaks *b* and *c* stem from hybridized O2*p*–transitonal metal 4*sp* band [33]. The two spectra show a difference in the relative height of the pre-peak with respect to the first peak *b*. The decrease in height for the pre-peak in the sample after 2000 cycles indicates the formation of oxygen vacancies in conjunction with the decrease in valence state, as observed from Co L-edge and Ni L-edge. This result agrees with the previously reported results for similar CoO_x materials [34,35]. The formation of oxygen vacancies and functional hydroxyl groups during long-term charge-discharge cycling is also validated by X-ray photoelectron spectroscopy (XPS) (see Fig. S4 in Supporting Information). Previous studies [36–38] showed that more oxygen vacancies and functional hydroxyl groups, which lead to increased carrier density (better electrical conductivity), facilitate the transport of charge carriers, thereby enhancing the capacitive storage of cycling Co_3O_4@$NiCo_2O_4$ nanoforests.

4. Conclusions

A coupled one-step solution and annealing process has been develpoped to synthesize hierarchical mesporous Co_3O_4@$NiCo_2O_4$ nanoforests on Ni foam for SC electrode applications. The synthesized Co_3O_4@$NiCo_2O_4$ nanoelectrode exhibits a dynamic capacitive storage behavior during charge-discharge cycling (from 0.73 F/cm^2 of the pristine state to the peak value of 1.12 F/cm^2 after 2000 cycles with only *ca.*1.8% loss compared to the peak capacitance after another 2000 cycles). We attribute such dynamic capacitive activation to (1) enlarged electroactive surface area through the formation of Co_3O_4@$NiCo_2O_4$ nanoforest core-shell structure and (2) enhanced electrical conductivity by forming oxygen vacancies and hydroxyl groups. The change in microstrcuture during charge-discharge cycling promote the transport of charge carriers, thereby enhancing the capacitive storage of cycling Co_3O_4@$NiCo_2O_4$ nanoforests. The discovered electrochemical induced microstructure change during charge-discharge cycling creates new opportunities for developing high performance sustainable energy storage devices.

Acknowledgements

This work was supported by the Beijing Nova Program (2010B008), Beijing Natural Science Foundation (2132014) and National Natural Science Foundation of China (11374027).

Appendix A. Supplementary data

Supplementary data associated with this article can be found, in the online version, at http://dx.doi.org/10.1016/j.electacta.2014.06.168.

References

[1] H. Nishide, K. Oyaizu, Science 319 (2008) 737.
[2] M. Armand, J.M. Tarascon, Nature 451 (2008) 652.
[3] P. Simon, Y. Gogotsi, Nat. Mater 7 (2008) 845.
[4] B.E. Conway, Electrochemical supercapacitors: Scientific fundamentals and technological applications, Kluwer Academic/Plenum Pub$lishers, New York, 1999.
[5] J.R. Miller, P. Simon, Science 321 (2008) 651.
[6] Y. Zhang, H. Feng, X.B. Wu, L.Z. Wang, A.Q. Zhang, T.C. Xia, H.C. Dong, X.F. Li, L.S. Zhang, International Journal of Hydrogen Energy 34 (2009) 4889.
[7] J.H. Zhu, J. Jiang, J.P. Liu, R.M. Ding, H. Ding, Y.M. Feng, G.M. Wei, X.T. Huang, J. Solid State Chem 184 (2011) 578.
[8] J.H. Kim, K. Zhu, Y.F. Yan, C.L. Perkins, A.J. Frank, Nano Lett 10 (2010) 4099.
[9] Z. Chen, V. Augustyn, J. Wen, Y.W. Zhang, M.Q. Shen, B. Dunn, Y.F. Lu, Adv.Mater. 23 (2011) 791.
[10] Y.C. Chen, Y.K. Hsu, Y.G. Lin, Y.K. Lin, Y.Y. Horng, L.C. Chen, K.H. Chen, Electrochim. Acta 56 (2011) 7124.
[11] J.G. Wang, Y. Yang, Z.H. Huang, F.Y. Kang, Electrochim. Acta 56 (2011) 9240.
[12] D.Q. Liu, Q. Wang, L. Qiao, F. Li, D.S. Wang, Z.B. Yang, D.Y. He, J. Mater. Chem 22 (2012) 483.
[13] H. Cheng, Z.G. Lu, J.Q. Deng, C. Chung, K. Zhang, Y.Y. Li, Nano Res 3 (2010) 895.
[14] X. Qing, S. Liu, K. Huang, K. Lv, Y. Yang, Z. Lu, D. Fang, X. Liang, Electrochim. Acta 56 (2011) 4985.
[15] R.B. Rakhi, W. Chen, D.k. Cha, H.N. Alshareef, Nano Lett 12 (2012) 2559.
[16] X.H. Xia, J.P. Tu, Y.Q. Zhang, Y.J. Mai, X.L. Wang, C.D. Gu, X.B. Zhao, RSC Adv 2 (2012) 1835.
[17] X.H. Xia, J.P. Tu, Y.Q. Zhang, X.L. Wang, C.D. Gu, X.B. Zhao, H.J. Fan, ACS Nano 6 (2012) 5531.
[18] X.H. Xia, J.P. Tu, Y.J. Mai, X.L. Wang, C.D. Gu, X.B. Zhao, J. Mater. Chem 21 (2011) 9319.
[19] B.R. Duan, Q. Cao, Electrochim. Acta 64 (2012) 154.
[20] H.W. Wang, Z.A. Hu, Y.Q. Chang, Y.L. Chen, H.Y. Wu, Z.Y. Zhang, Y.Y. Yang, J. Mater. Chem 21 (2011) 10504.
[21] X.Y. Liu, Y.Q. Zhang, X.H. Xia, S.J. Shi, Y. Lu, X. Li. Wang, C.D. Gu, J.P. Tu, J. Power. Sources 239 (2013) 157.
[22] H. Jiang, J. Ma, C.Z. Li, Chem. Commun 48 (2012) 4465.
[23] X.Y. Liu, S.J. Shi, Q.Q. Xiong, L. Li, Y.J. Zhang, H. Tang, C.D. Gu, X.L. Wang, J.P. Tu, ACS Appl. Mater. Interfaces 5 (2013) 8790.
[24] C.Z. Yuan, J.Y. Li, L.R. Hou, X.G. Zhang, L.F. Shen, X.W. Lou, Adv. Funct. Mater 22 (2012) 4592.
[25] C.H. An, Y.J. Wang, Y.N. Huang, Y.N. Xu, C.C. Xu, L.F. Jiao, H.T. Yuan, CrystEngComm 16 (2014) 385.
[26] Q.F. Wang, B. Liu, X.F. Wang, S.H. Ran, L.M. Wang, D. Chen, G.Z. Shen, J. Mater. Chem 22 (2012) 21647.
[27] C.T. Hsu, C.C. Hu, J. Power. Sources 242 (2013) 662.
[28] C.C. Hu, C.T. Hsu, K.H. Chang, H.Y. Hsu, J. Power. Sources 238 (2013) 180.
[29] R. Ding, L. Qi, H.Y. Wang, J Solid State Electrochem 16 (2012) 3621.
[30] M.H. Seo, M. Park, K.T. Lee, K. Kim, J.Y. Kim, J. Cho, Energy Environ. Sci. 4 (2011) 425.
[31] J. Graetz, C.C. Ahn, O.Y. Hao, P. Rez, B. Fultz, Phys. Rev. B 29 (2004) 235103.
[32] Z.L. Wang, J.S. Yin, Y.D. Jiang, Micron 31 (2000) 571.
[33] F.M.F. de Groot, M. Grioni, J.C. Fuggle, J. Ghijsen, G.A. Sawatzky, H. Petersen, Phys. Rev. B 40 (1989) 5715.

[34] Z. Zhang, Ultramicroscopy 107 (2007) 598.
[35] S. Stemmer, A. Sane, N.D. Browning, T.J. Mazanec, Solid State Ionics. 130 (2000) 71.
[36] X.H. Lu, G.M. Wang, T. Zhai, M.H. Yu, J.Y. Gan, Y.X. Tong, Y. Li, Nano Lett 12 (2012) 1690.
[37] X.H. Lu, G.M. Wang, S.L. Xie, J.Y. Shi, W. Li, Y.X. Tong, Y. Li, Chem. Commun 48 (2012) 7717.
[38] W.B. Hu, Y. Liu, R.L. Withers, T.J. Frankcombe, L.N.A. Snashall, M. Kitchin, P. Smith, B. Gong, H. Chen, J. Schiemer, F. Brink, J.W. Leung, Nat. Mater 12 (2013) 821.
[39] L. Yu, G.Q. Zhang, C.Z. Yuan, X.W. Lou, Chem. Commun. 49 (2013) 137.
[40] D.P. Cai, D.D. Wang, B. Liu, L.L. Wang, Y. Liu, H. Li, Y.R. Wang, Q.H. Li, T.H. Wang, ACS Appl. Mater. Interfaces 6 (2014) 5050.
[41] H.L. Wang, Q.M. Gao, J. Jiang, Small 7 (2011) 2454.